Supported Single Fe Atoms Prepared Via Atomic Layer Deposition for Catalytic Reactions

Xiaofeng Wang, ^{1,#} Baitang Jin, ¹ Ye Jin, ¹ Tianpin Wu, ² Lu Ma, ² and Xinhua Liang, ^{1,*}

¹ Department of Chemical and Biochemical Engineering, Missouri University of Science and Technology, Rolla, MO 65409, United States

² X-Ray Science Division, Advanced Photon Source, Argonne National Laboratory, 9700 S. Cass Ave., Argonne, Illinois, 60439, United States

Corresponding Author

* Email: <u>liangxin@mst.edu</u> (Xinhua Liang)

[#] Present address: College of Environmental Science and Engineering, Dalian Maritime University, Dalian 116026, China

Abstract

In this study, we report a general strategy to synthesize Fe single-atom catalysts (SACs) on various substrates (e.g., multi-walled carbon nanotubes, SiO₂, and TiO₂) with high Fe loading (> 1.5 wt.%) by atomic layer deposition (ALD) through optimization of ferrocene (Fe precursor) dose time. Fe/SiO₂ and Fe/TiO₂ SACs were used for CO oxidation reactions and catalytic degradation of a methylene blue (MB) solution, respectively. Compared with reported iron oxide catalysts, the efficiency of Fe/SiO₂ for CO oxidation was more than two orders of magnitude higher than the reported values. The photocatalysis experiment demonstrated that TiO₂ nanoparticles, deposited with two cycles of Fe ALD, showed the highest activity and had a more than six-fold photocatalytic

activity enhancement over pure TiO₂ for the degradation of MB. This universal method, optimized Fe ALD, expands the potential applications of Fe SACs on different substrates.

Keywords Iron, Single-atom catalyst, Atomic layer deposition, CO oxidation, Photocatalytic degradation

1. Introduction

Recently, metal single-atom materials have become to the forefront of international scientific research, within the field of a new hot spot, due to their unique properties and great potential for a variety of applications, especially in catalysis. However, single atoms are too mobile on supports since the surface free energy of metal increases dramatically when the metal particle size reduces to single-atom level. Thus, the metal single atoms are easy to sinter and aggregate during drying or calcination in the synthesis process, and it is a primary challenge to synthesize single-atom catalysts (SACs) with a high enough loading content for practical applications.

During the past few years, some studies have focused on the synthesis of single-atom materials and several new methods have been reported, including taking advantage of the unique properties of supports (e.g., photocatalysis of TiO₂ and defects of graphene),^{5, 7, 11-13} and enhancing metal-support interactions (e.g., Pt-CeO₂, Pd-C₃N₄, and Au-zeolite).^{6, 14, 15} In these methods, specific substrates need to be chosen, since strong interaction between metal single atoms and substrates is needed to prevent movement of single atoms on the substrates during preparation. Accordingly, though most of these SACs present excellent catalytic performance in various applications, the specific supports used for these methods limit the expansion of their applications. Moreover, the synthesis and applications of transition metal (e.g., Fe,^{3, 13, 16-18} Co,¹⁹⁻²² and Ni^{23, 24}) SACs have

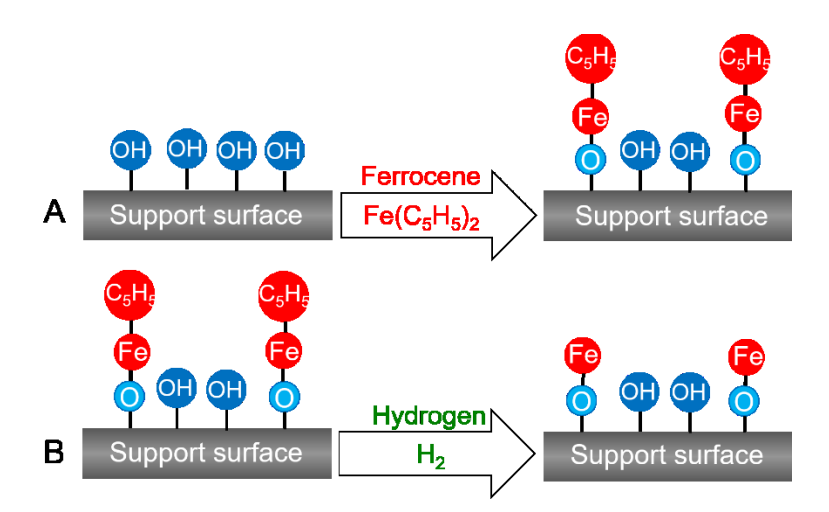
attracted increasing attention due to their low cost and activity that are comparable to that of noble metal catalysts. They have been used in catalytic oxidation, oxygen reduction reaction, and CO₂ reduction reactions.

Herein, we report a general atomic layer deposition (ALD) strategy to deposit well dispersed Fe single atoms on various substrates (e.g., multi-walled carbon nanotubes (MWCNTs), SiO₂, and TiO₂) with a high Fe loading of up to 1.78 wt.%, and describe the investigation of their catalytic performance in CO oxidation and degradation of methylene blue (MB). ALD is a surface controlled layer-by-layer gas phase coating process based on self-limiting surface reactions.^{25, 26} Pt and Pd SACs have been successfully deposited on graphene by using ALD. 11, 12 In this study, through optimizing the dose time of ferrocene (Fe(Cp)₂, precursor of Fe) and the number of Fe ALD cycles, we deposited Fe single atoms on different supports via Fe ALD. All prepared Fe samples are named and listed in Table S1. The formation of Fe single atoms was verified by Xray absorption spectroscopy (XAS) and high-angle annular dark-field scanning transmission electron microscopy (HAADF-STEM). The activities of Fe/SiO₂ and Fe/TiO₂ catalysts were evaluated by CO oxidation reactions and catalytic degradation of a MB solution under UV light, respectively, as two examples of the applications of Fe SACs. The results showed that 25c-Fe/SiO₂ SAC was much more active than the reported iron oxide catalysts, and the 2c-Fe/TiO₂ sample had a more than six-fold photocatalytic activity enhancement over pure TiO₂ for the degradation of MB.

2. Experimental

2.1. Catalysts preparation

Fe single atoms were deposited on MWCNTs (US Nano Inc), SiO₂ nanoparticles (NPs, 20-30 nm, US Nano Inc), and TiO₂ NPs (DT 51, 100% anatase, ~80 m²/g, Cristal Inc) by ALD using ferrocene and hydrogen (H₂, 99.9%, Airgas) as precursors in a fluidized bed reactor, as schematically shown in Figure S1. The reactor is described in detail elsewhere.^{27, 28} All of the chemicals were used, as received, without any treatment. For a typical cycle, 5 g of substrate were loaded into the reactor. The reaction temperature was 400 °C. Before a reaction, the substrates were degassed at 150 °C for 10 hr. During the ALD process, the solid ferrocene (~ 0.2 g) was loaded into a heated bubbler (115 °C) and carried by nitrogen (N₂, 99.9% Airgas) into the reactor. Fe(Cp)₂ and H₂ were fed separately through a distributor plate. The particle substrates were fully fluidized, with the gas flow rate controlled by mass flow controllers. The reactor was also subjected to vibration from vibrators to improve the quality of particle fluidization during the ALD coating process.^{29, 30} N₂ was used as a flush gas to remove unreacted precursors and any byproducts during the reaction. A typical coating cycle involved the following steps: ferrocene dose, N₂ purge, evacuation; H₂ dose, N₂ purge, evacuation. The proposed two half-reactions are presented in Scheme 1.



Scheme 1. Reaction scheme for Fe ALD half-reactions.

In order to compare the activity of Fe/SiO₂ SACs with iron oxide catalysts (Fe₂O₃), a Fe₂O₃/SiO₂-IW catalyst was prepared by an incipient wetness technique (impregnation method) as a reference.³¹ First, Fe(NO₃)₃ was dissolved in distilled water and, then, SiO₂ NPs were added to the solution. After the solution was dried at 100 °C for 12 hr, the particles were calcined in air at 400 °C for 5 hr, and the Fe₂O₃/SiO₂-IW catalyst was obtained. The Fe loading amount was 1.5 wt.%., and the catalyst was used for CO oxidation reaction directly.

2.2. Characterizations

The Fe mass fractions of prepared Fe samples, with different Fe ALD cycles, were measured by inductively coupled plasma atomic emission spectroscopy (ICP-AES). The Fe supported on MWCNTs, SiO₂, and TiO₂ NPs were directly observed by FEI Tecnai F20 high-resolution transmission electron microscopy (TEM) at 200 kV. High-angle annular dark-field scanning transmission electron microscopy (HAADF-STEM) analysis, operated at 100 kV, was performed using Nion UltraSTEM 100. X-ray absorption spectroscopy (XAS) was applied to verify the composition of Fe on the MWCNTs, SiO₂ and TiO₂ NPs. X-ray photoelectron spectroscopy (XPS) analysis was performed for 25c-Fe/SiO₂ samples before and after CO oxidation reactions. The crystal structures of Fe/TiO₂ and 25c-Fe/SiO₂ samples before and after CO oxidation were detected by X-ray powder diffraction (XRD). The Raman spectra of TiO₂ and Fe/TiO₂ samples were collected using a Horiba-Jobin Yvon LabRam spectrometer, and the photoluminescence (PL) spectra of TiO₂ and Fe/TiO₂ samples were recorded with a HORIBA FL3-22 spectrometer (HORIBA, Edison, NJ) to investigate and determine the recombination of photo-generated e⁻/h⁺ pairs in the samples. UV-visible diffuse reflectance spectra (DRS) of Fe/TiO₂ samples were obtained with a UV-visible spectrophotometer (Varian Cary 5), and BaSO₄ was used as an

absorbance standard in the UV-visible absorbance experiment. The details of characterization are described in Supporting Information (SI).

2.3. CO oxidation reaction

The CO oxidation reactions were performed in a fixed bed quartz reactor with quartz wool supporting the catalysts. In a typical run, 50 mg samples were used in each reaction. A gas mixture, with 2 mL/min (sccm) CO, 2/10/20 sccm O₂, and rest of N₂, was introduced into the reactor for CO oxidation reaction. The total flow rate was 50 sccm. Reaction temperatures ranged from 200 °C to a temperature at which the CO conversion reached 100%. Reaction products were analyzed by an online gas chromatograph (SRI 8610C), equipped with a 6-foot HAYESEP D column, a 6-foot molecular sieve 13X column, and a FID detector. After reaction, the catalyst was directly used for the following cycling tests, when applicable. In addition, in order to verify the long-term stability of the Fe/SiO₂ sample, the CO oxidation reaction over 25c-Fe/SiO₂ (50 mg) was carried out for more than 400 hr at 550 °C. The Fe₂O₃/SiO₂-IW catalyst was also used in CO oxidation, as a reference.

2.4. Photocatalytic activity measurement

MB solution was used to evaluate the photocatalytic activities of pure TiO₂ and Fe/TiO₂ particles, as previously described in detail.³² Briefly, 0.1 g of sample was added in a 100 mL, 10 ppm MB solution. First, the suspension solution was stirred in the dark for 60 min to achieve adsorption/desorption equilibrium. Then, a UV lamp was used for 360 nm of UV irradiation, and ~1 mL test samples were taken, at certain time intervals, from the main solution for analysis at a

664 nm wavelength. Changes in the concentration of MB in the main solution were recorded over a period of reaction time.

3. Results and discussion

First, different cycles (2-10 cycles) of Fe ALD were deposited on 3 g of MWCNTs in a fluidized bed reactor (schematically shown in Figure S1) using ferrocene (Fe(Cp)₂) and H₂ as precursors (all sample names are listed in Table S1). The dose time of Fe(Cp)₂ was 300 s. As shown in Figures 1a and S2, some bright dots of atomic size that were scattered on MWCNTs after ten Fe ALD cycles, are highlighted by the yellow circles. Each dot representes an individual Fe atom, which proves that Fe single atoms were deposited on MWCNTs successfully with 0.36 wt.% Fe loading, as determined by ICP-AES (Figure S3a). Then, 1-15 cycles of Fe ALD were applied on 3 g of TiO₂ NPs, using the same dose time (300 s) of Fe(Cp)₂. The Fe content was up to 1.78 wt.% in 15c-Fe/TiO₂ samples (Figure S3b). As presented in Figure 1b, several bright dots that were observed on TiO₂ NPs, after 15 cycles of Fe ALD, indicated the formation of Fe single atoms on TiO₂ NPs. It is also noted that the Fe content in the Fe/TiO₂ particles increased almost linearly with an increase in the number of ALD cycles after 15 cycles of Fe ALD, which indicated that the Fe deposition was uniform in every ALD cycle (Figure S3b). Fe single atoms were also deposited on SiO₂ via ALD to prove that Fe ALD is a universal method to synthesize Fe SACs on various substrates. As presented in Figure 1c, there are no Fe NPs observed on SiO₂ NPs after 25 cycles of Fe ALD, with 1.49 wt.% Fe (Figure S3c), which indicate the formation of Fe single atoms on SiO₂ NPs. In contrast, when the Fe(Cp)₂ dose time increased to 600 s, Fe NPs were formed on SiO₂ NPs, after only five cycles of Fe ALD, and the average particle size of Fe NPs was around 1.5 nm, as shown in Figure 1d.

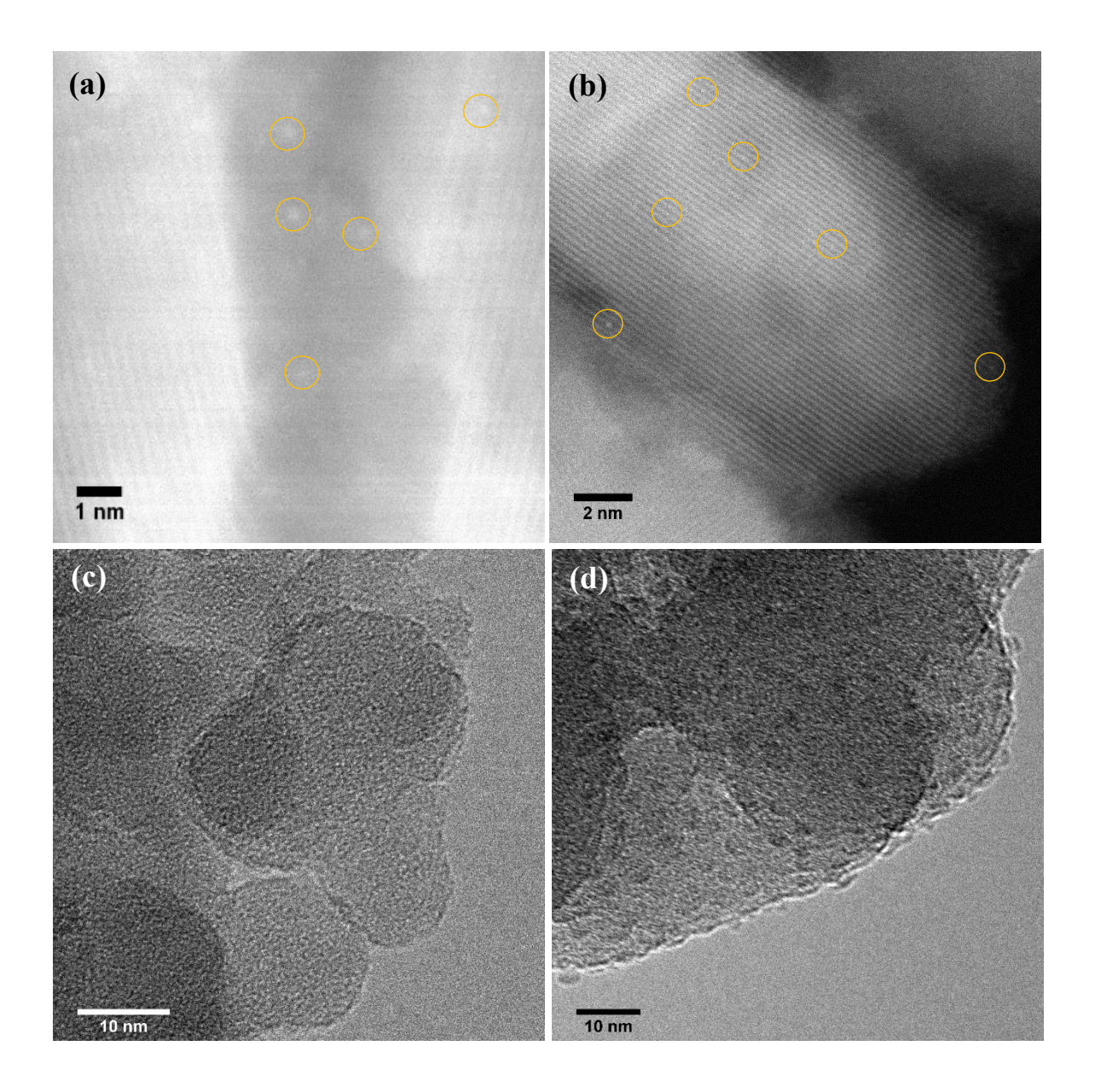


Figure 1. HAADF-STEM images of (a) 10c-Fe/MWCNTs and (b) 15c-Fe/TiO₂, and TEM images of (c) 25c-Fe/SiO₂ and (d) 5c-Fe/SiO₂-600s samples.

In order to further verify the formation of the Fe single-atom structure, XAS analyses were conducted for Fe/MWCNTs, Fe/TiO₂, and Fe/SiO₂ samples. As shown in Figure 2a, the Fe K-edge of X-ray absorption near the edge structure spectroscopy (XANES) in Fe/MWCNTs, Fe/TiO₂, and

Fe/SiO₂ samples exhibited a near-edge structure similar to that of the Fe₂O₃, but it was very different from those of Fe foil and FeO, indicating that Fe was a single atom and oxidized upon air exposure. After fitting and calculating, both samples were oxidized to the extent of a mixture of ~85% Fe³⁺ and ~15% Fe²⁺ (Table S2). Extended X-ray absorption fine structure spectroscopy (EXAFS) of the Fe K-edge showed that there was only one notable peak in the region of 1 to 2 Å from the Fe-O contribution, and no peak in the region of 2 to 3 Å from the Fe-Fe contribution, confirming the sole presence of dispersed Fe atoms in all Fe samples (Figure 2b). These results indicated that Fe single atoms would form with a short Fe(Cp)₂ dose time, but if the dose time was extended, Fe NPs would form on the substrates instead of single atoms. It could be explained that when more Fe(Cp)₂ molecules entered the ALD reactor with a longer Fe precursor dose time, there was a higher possibility of the formation of Fe NPs in each Fe ALD cycle, which could be changed from Fe single atoms. So Fe(Cp)₂ dose time played an important role in the formation of Fe single atoms during the ALD process.

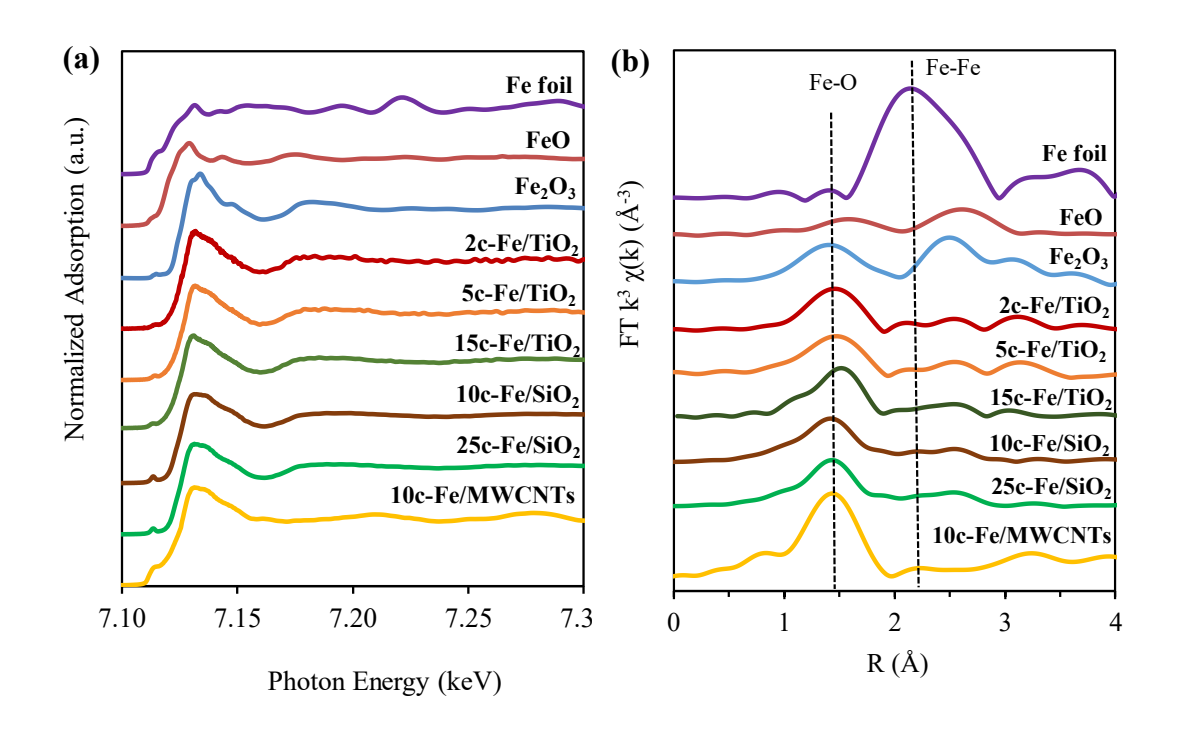


Figure 2. (a) Fe K-edge XANES (7.0-7.7 keV) and (b) Fourier transformed (FT) k^3 -weighted $\chi(k)$ -function of EXAFS spectra of 10c-Fe/MWCNTs, Fe/TiO₂ and Fe/SiO₂ samples in comparison to Fe foil, FeO, and Fe₂O₃.

ALD is a surface-controlled process based on self-limiting surface reactions. Through making use of the unique advantage of ALD, Fe single atoms are deposited on MWCNTs, SiO₂, and TiO₂ by controlling the Fe(Cp)₂ dose time. Therefore, Fe ALD has been demonstrated to be a general method that can be used to preparare Fe single-atom materials on various supports, including inorganic non-metallic materials, metal oxides, and carbon materials. In comparison to other methods (e.g., pyrolysis and ionic exchange),³³ our results indicate that there is no limitation of supports when ALD is used for Fe SACs preparation.

The catalytic activity of Fe/SiO₂ SACs was evaluated by CO oxidation reaction. Figure 3a presented the effect of different CO/O₂ molar ratios on CO oxidation over the 25c-Fe/SiO₂ catalyst. With an increase in the O₂ flow rate, CO conversion reached 100% in a lower temperature. The temperatures for 100% conversion were 570 °C, 460 °C, and 410 °C, with a CO:O₂ ratio of 1:1, 1:5, and 1:10, respectively. This indicates that a CO molecule contacted and reacted with O₂ on the surface of Fe single atoms more easily when the O₂ concentration in the gas stream was higher. Generally, catalytic activity is evaluated by turnover frequency (TOF), which is related to the metal dispersion of catalysts. Since the 25c-Fe/SiO₂ was a single-atom catalyst, the Fe dispersion was assumed to be 100%. Thus, the TOF was 0.67 min⁻¹ when the CO conversion reached 10%, with a CO:O₂ ratio of 1:10 at 360 °C. Compared with the reported Fe₂O₃ catalysts, ³⁴⁻³⁸ the specific rate of 25c-Fe/SiO₂ (46.30 mL_{CO} g_{Fe}⁻¹s⁻¹) was more than two orders of magnitude higher than the reported values (Table S3) and, therefore, our 25c-Fe/SiO₂ catalyst is much more efficient than

other Fe-based catalysts in the reaction of CO oxidation. This could be due to the fact that each Fe atom worked as an active site for the 25c-Fe/SiO₂ catalyst and, thereby, the catalytic efficiency increased greatly. Generally, for CO oxidation, the Langmuir-Hinshelwood (LH) mechanism and Eley-Rideal (ER) mechanism are two common reaction mechanisms. According to previous theoretical study,³⁹ the CO oxidation by adsorbed O₂ on Fe single atom catalysts prefers to perform via the ER mechanism since the energy barrier is low through density functional theory (DFT) calculations. Thus, in this study, first O₂ molecules were adsorbed on Fe single atoms and activated, i.e., the adsorbed atomic O, then CO molecules reacted with them and produced CO₂. The two reaction steps are involved as follows: ³⁹

$$O_{2(ad)} + CO_{(gas)} \rightarrow O_{(ad)} + O_{(ad)} + CO_{(gas)} \rightarrow O_{(ad)} + CO_{2(gas)}$$
 (1)

$$CO_{(gas)} + O_{(ad)} \rightarrow CO_{2(gas)}$$
 (2)

When the concentration of O₂ in the gas stream was high, more O₂ could be used for CO oxidation and more Fe single atoms would be used to catalyze CO oxidation. Thus, 100% of CO conversion was achieved at a relatively low temperature with the CO:O₂ ratio of 1:10, as shown in Figure 3a. In comparison, the catalytic CO oxidation utilizing Fe₂O₃ can be divided into two steps. First, Fe₂O₃ loses one oxygen atom and catalyzes CO to form CO₂ and, then, the generated FeO is further oxidized by O₂.⁴⁰ As a control, the activities of SiO₂ NPs were also evaluated by CO oxidation (Figure S4), and the CO conversion was very low, so the SiO₂ support did not influence the catalytic performance of the 25c-Fe/SiO₂ catalyst. In order to compare the activity of the 25c-Fe/SiO₂ catalyst with that of Fe₂O₃, we prepared a Fe₂O₃/SiO₂-IW catalyst by an incipient wetness method and used it in the CO oxidation reaction as well. As shown in Figure S5, its activity was much lower than that of the 25c-Fe/SiO₂ single-atom catalyst.

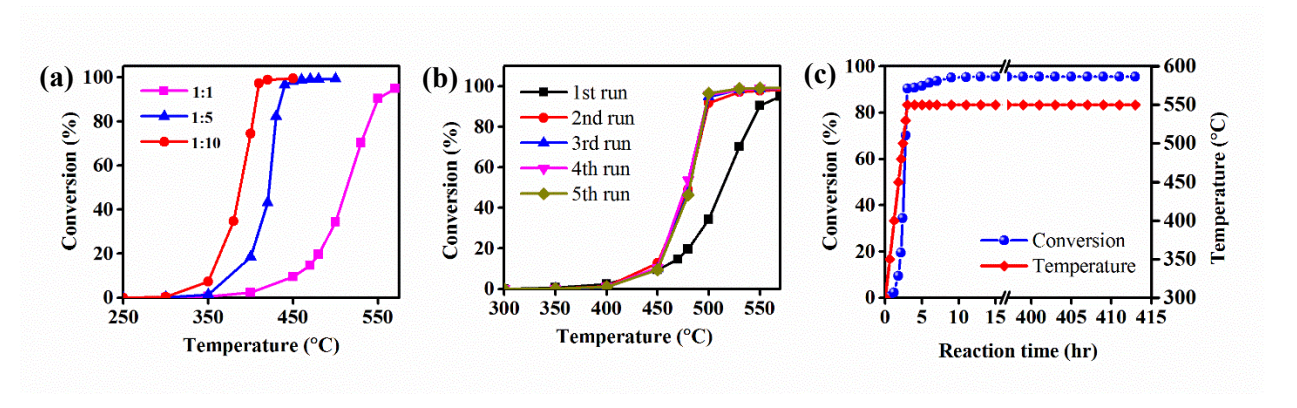


Figure 3. (a) Effect of different molar ratios of CO to O₂ on CO conversion over 25c-Fe/SiO₂ catalyst. The flow rate of CO was kept at 2 sccm, and that of O₂ was 2 sccm, 10 sccm, and 20 sccm in each run; (b) cycling stability test and (c) long-term stability test of 25c-Fe/SiO₂ SAC for CO oxidation (2 sccm CO, 2 sccm O₂, and 46 sccm N₂).

The stability of the 25c-Fe/SiO₂ catalyst was evaluated by cycling tests and, as shown in Figure 3b, five cycles of CO oxidation reactions were applied for the 25c-Fe/SiO₂ SAC catalyst and the catalyst showed higher activity in the run 2-5 than in the first run. This could be attributed to the fact that some functional groups were still on the Fe atoms, which did not compeltely react with H₂ during the ALD process, and these Fe atoms were not involved in the CO oxidation reaction in the first run. However, these functional groups reacted with O₂ during the first run and, thereby, the Fe atoms could be used in the following runs. Thus, the catalytic activity improved in the run 2-5. In order to verify the hypothesis, XPS analysis was performed for the 25c-Fe/SiO₂ samples before and after CO oxidation. It is noted that there was a broad peak of C(1s) located at 287-295 eV for the as-prepared 25c-Fe/SiO₂ sample, and the peak disapeared after the CO oxidation reaction (as shown in Figure S6a). It should be assigned to the remaining functional groups on the Fe atom surface after the ALD process. In the CO oxidation reaction, these functional groups reacted with O₂, so there was no such peak observed for Fe/SiO₂ after CO oxidation reactions.

As shown in Figure 3c, a long-term stability test was performed. Since the CO conversion reached 100% at 550 °C, the reaction was kept running for more than 400 hours at 550 °C, and no decrease in CO conversion was observed. This indicates that the 25c-Fe/SiO₂ catalyst was still very reactive and durable under severe conditions, e.g., high temperature. The state of Fe did not change during the long-term test based on XPS and XRD results (Figures 4, S6b, and S7). In comparision with the reported catalysts (e.g., Au, 41 Pd, 42 and Co₃O₄ 43), the 25c-Fe/SiO₂ SAC catalyst retained high activity for a longer time at a higher temperature, with these properties being vital for practical applications (Table S4). In general, metal/metal oxide NPs or sub-nanometer particles remain stable on the surface of supports at low temperatures, and do not aggregate to form larger particles. It is difficult, however, to dissociate O₂ molecules at low temperatures owing to a lack of enough energy after O₂ molecules adsorb on metal/metal oxide particles for CO oxidation, which results in deactivation of catalysts. 42 On the other side, there is a high possibility that the metal/metal oxide catalysts will aggregate at high reaction temperatures, which will lead to deactivation as well. ⁴¹ In this study, the 25c-Fe/SiO₂ SAC is very stable at high temperatures. So, this is a potential and promising alternative for catalytic oxidation of CO exhaust from vehicles due to its outstanding performance.

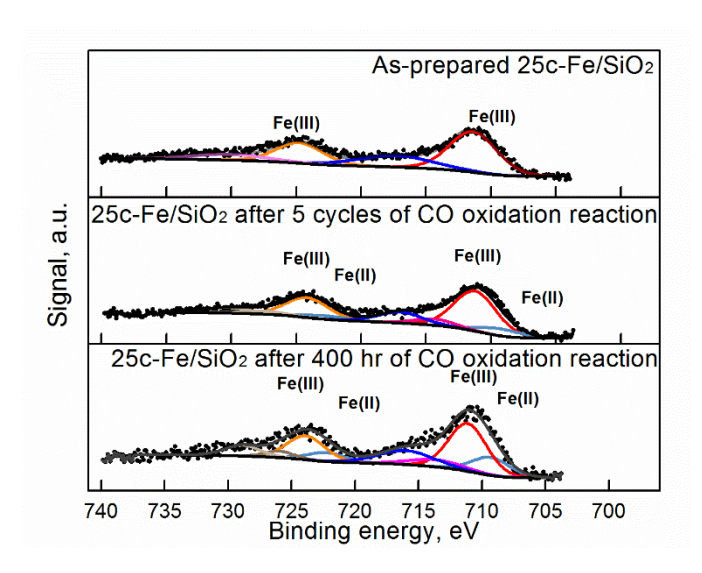


Figure 4. High resolution XPS spectra of Fe (2p) for 25c-Fe/SiO₂ samples before and after CO oxidation reactions.

In addition to the application of CO removal, the Fe single atom samples were used in photocatalytic degradation of MB. As shown in Figures 5 and S8, after Fe ALD deposition without further treatment, the Fe/TiO₂ samples with 1-5 Fe ALD cycles showed a higher photocatalytic efficiency than that of pure TiO₂, and the apparent kinetic constants (k_{app}) of the 2c-Fe/TiO₂ sample reached a maximum value (0.155 min⁻¹), so that its activity exceeded that of pure TiO₂ by a factor of more than six times. Liu and Chen⁴⁴ reported an increase of only 1.62 times of photocatalytic activity, as compared to undoped TiO₂ for a similar system. In addition, Pt ALD and CeO₂ ALD were reported as being applied to improve TiO₂ photoactivity, but this showed only 3 and 3.3 times increase in photocatalytic activity, as compared to pure TiO₂, respectively.^{32, 45} More importantly, Fe is much cheaper and more economic for large-scale production compared to Pt. Thus, in comparison with other methods, Fe ALD is a promising strategy that can enhance Fe/TiO₂ photocatalytic performance (Table S5). The much higher photoactivity of 2c-Fe/TiO₂ in this work, than that of TiO₂, can be due to the following several factors.

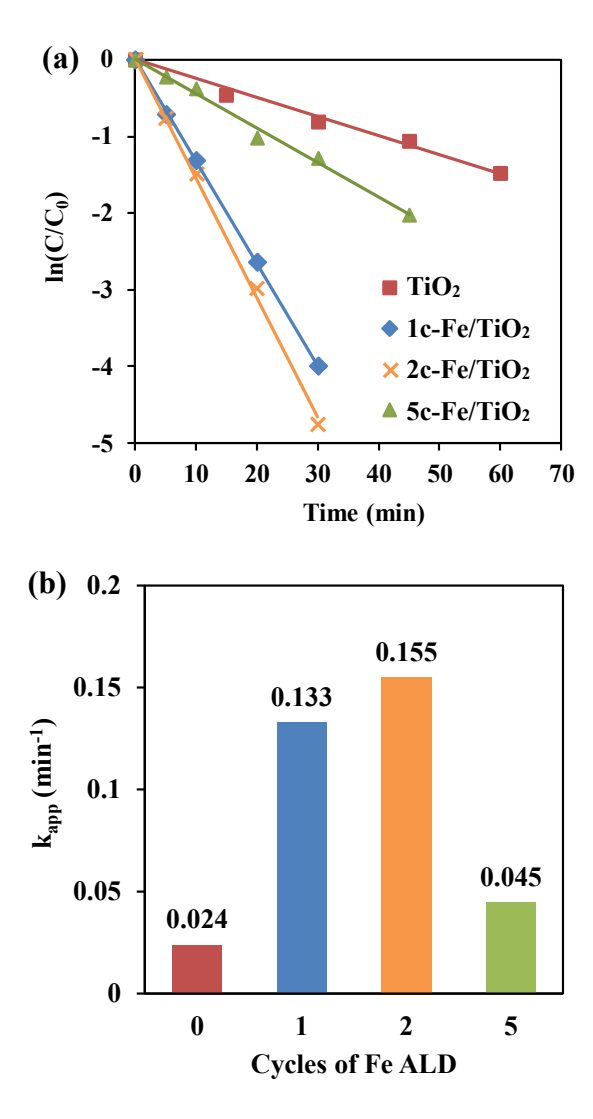


Figure 5. (a) Relative methylene blue concentration as a function of UV irradiation time over different samples, and (b) apparent kinetic constant (k_{app} , min^{-1}) as a function of Fe/TiO₂ catalysts with different numbers of Fe ALD cycles.

First, Fe³⁺ ions could improve the intensity of absorption in the UV-visible light region and make a red shift in the band gap transition of the 2c-Fe/TiO₂ sample. This can induce more photogenerated e⁻ and h⁺ to participate in the photocatalytic reactions.⁴⁶ Based on the UV-visible DRS for pure TiO₂ and Fe/TiO₂ catalysts (Figures S9-S11), the band gap was calculated. As shown in

Figure 6, the band gap energy values decreased from 3.22 eV to 3.03 eV, along with the 0 to 5 increase in the number of Fe ALD cycles. Increasing the Fe content in TiO₂ shifted the band gap energy toward longer wavelengths due to the creation of trap levels between the conduction and valence bands of TiO₂.^{47, 48} More cycles of Fe ALD would provide more trap centers and, thereby, lead to a lager reduction in the band gap.

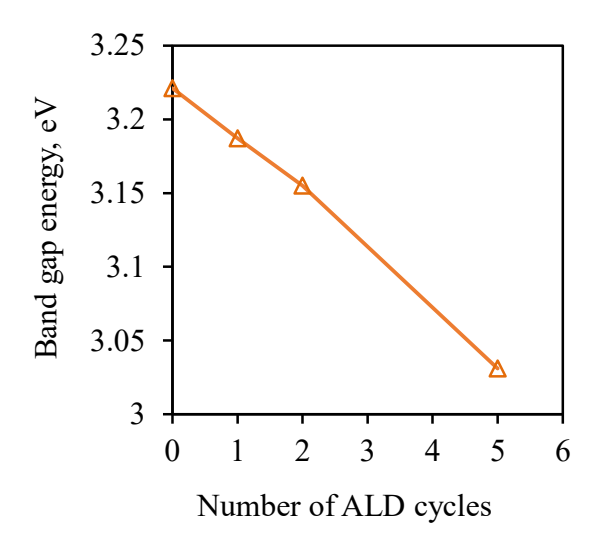


Figure 6. Band gap energy of TiO₂ and Fe/TiO₂ samples.

Second, Fe atoms can work as an e⁻/h⁺ pair trap to suppress the recombination of e⁻/h⁺ pairs and enhance lifetimes of e⁻ and h⁺, which can improve the photocatalytic activity of Fe/TiO₂ samples as well. In order to investigate the recombination rate of e⁻/h⁺ pairs in all catalysts, Raman and PL were performed. As shown in Figure 7a, all samples showed three major Raman bands at 397 cm⁻¹, 517 cm⁻¹, and 640 cm⁻¹, which are attributed to the Raman-active modes of the TiO₂ anatase phase with the symmetries of B1g, A1g, and Eg, respectively.⁴⁹ It is noted that the baseline of 1c-Fe/TiO₂, 2c-Fe/TiO₂, and 5c-Fe/TiO₂ kept increasing from 300 cm⁻¹ to 1000 cm⁻¹, which resulted from a fluorescence effect after Fe deposition on TiO₂ NPs. Thus, PL analyses of the TiO₂ and Fe/TiO₂ samples were carried out to further study the fluorescence effect and recombination

rate of e⁻/h⁺ pairs (Figure 7b). The only peak at 432 nm corresponded to the reflection from the anatase phase of TiO₂. With an increase in the number of Fe ALD cycles, the PL intensity greatly decreased, which indicated that the separation efficiency of e⁻/h⁺ pairs improved for Fe/TiO₂ samples, and could have resulted from an increase of the number of trap centers.⁵⁰ However, with an increase in the Fe content in samples, Fe atoms can serve not only as an e⁻/h⁺ trap but also as a recombination center. In this study, the photocatalytic activity decreased greatly, compared to that of the 2c-Fe/TiO₂ catalyst, when the Fe concentration increased. This was attributed to the fact that more Fe atoms played a role as e⁻/h⁺ recombination centers and improved the e⁻/h⁺ recombination rate. In addition, no peak was presented that corresponded to Fe in both Raman and PL analyses, which could be due to the low content and ultra-small size of Fe in the samples.

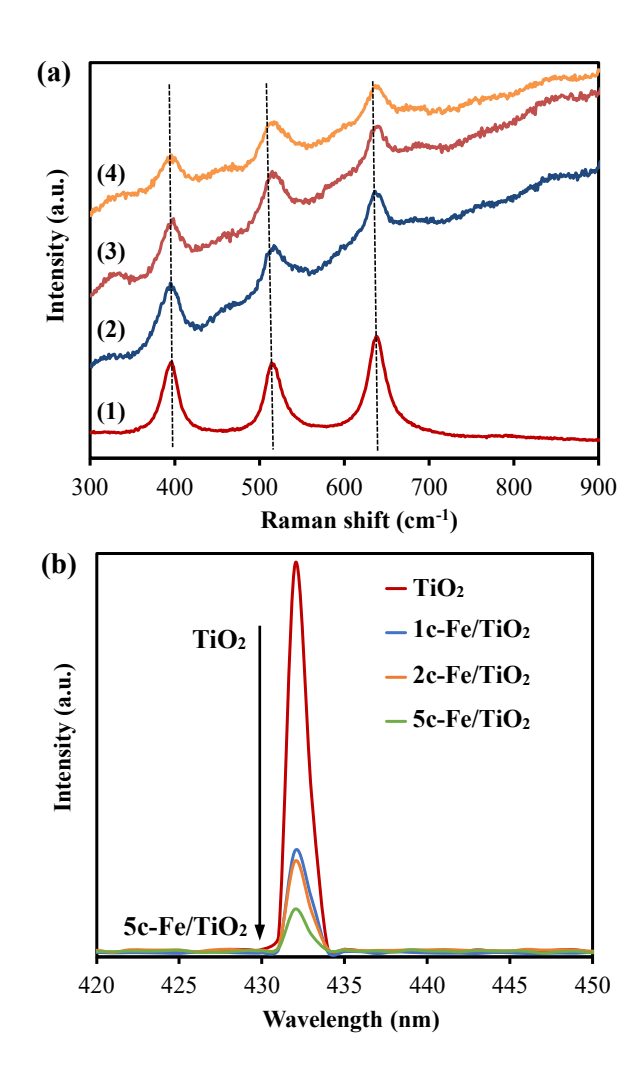


Figure 7. (a) Raman spectra of (1) TiO₂, (2) 1c-Fe/TiO₂, (3) 2c-Fe/TiO₂, and (4) 5c-Fe/TiO₂, and (b) photoluminescence (PL) spectra of TiO₂ and Fe/TiO₂ samples excited at 280 nm.

Last, the atomic size and uniform dispersion of Fe on TiO₂ surface is another important factor that influences photocatalytic efficiency. Fe ALD took full advantage of the large surface area of TiO₂, and Fe single atoms (~0.2 nm) were highly dispersed on TiO₂. Thus, Fe³⁺ ions worked as many as possible e⁻/h⁺ traps in Fe/TiO₂ samples, which led to the fact that the recombination of e⁻ and h⁺ decreased and photocatalytic activity drastically improved. In addition, according to XRD analysis, the TiO₂ in all samples remained anatase structure after Fe ALD and no peak

corresponded to the reflections from Fe, which indicates that the crystal structure did not affect the improvement in photocatalytic activity for the 2c-Fe/TiO₂ sample (Figure S12). All factors mentioned above worked collectively and resulted in improved photocatalytic activity of 2c-Fe/TiO₂.

4. Conclusions

Fe single atoms were deposited on MWCNTs, SiO₂, and TiO₂ NPs by Fe ALD. HAADF-STEM and XAS analysis proved the existence of Fe single atoms on MWCNTs, TiO₂, and SiO₂ NPs. Ferrocene dose time is the dominating factor in the preparation of Fe single atoms on substrates. The 25c-Fe/SiO₂ SAC showed ultra-high activity and an excellent long-term stability at a high temperature in the reaction of CO oxidation. The 2c-Fe/TiO₂ catalyst presented the highest photocatalytic activity and had a more than six-fold photocatalytic activity enhancement over pure TiO₂ for the degradation of MB. This study proves that Fe ALD is a universal strategy to prepare Fe single-atom materials on various kinds of substrates.

Supporting Information

Details of XAS, XPS, XRD, and Raman characterizations; Band gap calculation; Supporting figures and tables

Conflict of interest

The authors declare no competing financial interest.

Acknowledgement

This work was supported in part by the National Science Foundation grant NSF 1803812. The authors thank Dr. Jingjing Qing at the Materials Research Center at Missouri University of Science and Technology for TEM analysis, and Katia March at LeRoy Eyring Center for Solid State Science at Arizona State University for HAADF-STEM analysis. The authors also thank Naveen K. Mahenderkar and Prof. Jay A. Switzer in the Department of Chemistry for the assistance with diffuse reflectance UV-vis measurement, and Jincheng Bai and Prof. Richard Brow in the Department of Materials Science and Engineering at Missouri University of Science and Technology for the assistance with Raman and photoluminescence analysis. Use of the Advanced Photon Source (9-BM) by Argonne National Laboratory, was supported by the U.S. Department of Energy, Office of Basic Energy Sciences, under Contract No. DE-AC02-06CH11357.

References

- 1. Qiao, B.; Wang, A.; Yang, X.; Allard, L. F.; Jiang, Z.; Cui, Y.; Liu, J.; Li, J.; Zhang, T. Single-atom catalysis of CO oxidation using Pt₁/FeO_x. *Nature Chemistry* 2011, 3, 634-641.
- 2. Kyriakou, G.; Boucher, M. B.; Jewell, A. D.; Lewis, E. A.; Lawton, T. J.; Baber, A. E.; Tierney, H. L.; Flytzani-Stephanopoulos, M.; Sykes, E. H. Isolated metal atom geometries as a strategy for selective heterogeneous hydrogenations. *Science(Washington)* 2012, 335, 1209-1212.
- 3. Deng, D.; Chen, X.; Yu, L.; Wu, X.; Liu, Q.; Liu, Y.; Yang, H.; Tian, H.; Hu, Y.; Du, P. A single iron site confined in a graphene matrix for the catalytic oxidation of benzene at room temperature. *Science Advances* 2015, 1, e1500462.
- 4. Ding, K.; Gulec, A.; Johnson, A. M.; Schweitzer, N. M.; Stucky, G. D.; Marks, L. D.; Stair, P. C. Identification of active sites in CO oxidation and water-gas shift over supported Pt catalysts. *Science* 2015, 350, 189-192.

- 5. Liu, P.; Zhao, Y.; Qin, R.; Mo, S.; Chen, G.; Gu, L.; Chevrier, D. M.; Zhang, P.; Guo, Q.; Zang, D. Photochemical route for synthesizing atomically dispersed palladium catalysts. *Science* 2016, 352, 797-800.
- 6. Jones, J.; Xiong, H.; DeLaRiva, A. T.; Peterson, E. J.; Pham, H.; Challa, S. R.; Qi, G.; Oh, S.; Wiebenga, M. H.; Hernández, X. I. P. Thermally stable single-atom platinum-on-ceria catalysts via atom trapping. *Science* 2016, 353, 150-154.
- 7. Cheng, N.; Stambula, S.; Wang, D.; Banis, M. N.; Liu, J.; Riese, A.; Xiao, B.; Li, R.; Sham, T.-K.; Liu, L.-M. Platinum single-atom and cluster catalysis of the hydrogen evolution reaction.

 Nature Communications 2016, 7, Article No. 13638.
- 8. Li, J.; Guan, Q.; Wu, H.; Liu, W.; Lin, Y.; Sun, Z.; Ye, X.; Zheng, X.; Pan, H.; Zhu, J.; Chen, S.; Zhang, W.; Wei, S.; Lu, J. Highly Active and Stable Metal Single-Atom Catalysts Achieved by Strong Electronic Metal-Support Interactions. *Journal of the American Chemical Society* 2019, 141, 14515-14519.
- 9. Zhang, J.; Zhao, Y.; Guo, X.; Chen, C.; Dong, C.-L.; Liu, R.-S.; Han, C.-P.; Li, Y.; Gogotsi, Y.; Wang, G. Single platinum atoms immobilized on an MXene as an efficient catalyst for the hydrogen evolution reaction. *Nature Catalysis* 2018, 1, 985-992.
- 10. Chen, W.; Pei, J.; He, C.-T.; Wan, J.; Ren, H.; Wang, Y.; Dong, J.; Wu, K.; Cheong, W.-C.; Mao, J.; Zheng, X.; Yan, W.; Zhuang, Z.; Chen, C.; Peng, Q.; Wang, D.; Li, Y. Single Tungsten Atoms Supported on MOF-Derived N-Doped Carbon for Robust Electrochemical Hydrogen Evolution. *Advanced Materials* 2018, 30, 1800396.
- 11. Yan, H.; Cheng, H.; Yi, H.; Lin, Y.; Yao, T.; Wang, C.; Li, J.; Wei, S.; Lu, J. Single-atom Pd₁/graphene catalyst achieved by atomic layer deposition: remarkable performance in selective

- hydrogenation of 1, 3-butadiene. *Journal of the American Chemical Society* 2015, 137, 10484-10487.
- 12. Sun, S.; Zhang, G.; Gauquelin, N.; Chen, N.; Zhou, J.; Yang, S.; Chen, W.; Meng, X.; Geng, D.; Banis, M. N.; Li, R.; Ye, S.; Knights, S.; Botton, G. A.; Sham, T.-K.; Sun, X. Single-atom Catalysis Using Pt/Graphene Achieved through Atomic Layer Deposition. *Scientific Reports* 2013, 3, 1775.
- 13. Chen, X.; Yu, L.; Wang, S.; Deng, D.; Bao, X. Highly active and stable single iron site confined in graphene nanosheets for oxygen reduction reaction. *Nano Energy* 2017, 32, 353-358.
- 14. Vilé, G.; Albani, D.; Nachtegaal, M.; Chen, Z.; Dontsova, D.; Antonietti, M.; López, N.; Pérez Ramírez, J. A stable single site palladium catalyst for hydrogenations. *Angewandte Chemie International Edition* 2015, 54, 11265-11269.
- 15. Yang, M.; Li, S.; Wang, Y.; Herron, J. A.; Xu, Y.; Allard, L. F.; Lee, S.; Huang, J.; Mavrikakis, M.; Flytzani-Stephanopoulos, M. Catalytically active Au-O (OH) x-species stabilized by alkali ions on zeolites and mesoporous oxides. *Science* 2014, 346, 1498-1501.
- 16. Ma, W.; Mao, J.; Yang, X.; Pan, C.; Chen, W.; Wang, M.; Yu, P.; Mao, L.; Li, Y. A single-atom Fe-N₄ catalytic site mimicking bifunctional antioxidative enzymes for oxidative stress cytoprotection. *Chemical Communications* 2019, 55, 159-162.
- 17. Gu, J.; Hsu, C.-S.; Bai, L.; Chen, H. M.; Hu, X. Atomically dispersed Fe³⁺ sites catalyze efficient CO₂ electroreduction to CO. *Science* 2019, 364, 1091.
- 18. Jiang, R.; Li, L.; Sheng, T.; Hu, G.; Chen, Y.; Wang, L. Edge-Site Engineering of Atomically Dispersed Fe-N₄ by Selective C-N Bond Cleavage for Enhanced Oxygen Reduction Reaction Activities. *Journal of the American Chemical Society* 2018, 140, 11594-11598.

- 19. Mao, J.; He, C.-T.; Pei, J.; Chen, W.; He, D.; He, Y.; Zhuang, Z.; Chen, C.; Peng, Q.; Wang, D.; Li, Y. Accelerating water dissociation kinetics by isolating cobalt atoms into ruthenium lattice.

 Nature Communications 2018, 9, 4958.
- 20. Fei, H.; Dong, J.; Arellano-Jiménez, M. J.; Ye, G.; Kim, N. D.; Samuel, E. L.; Peng, Z.; Zhu, Z.; Qin, F.; Bao, J. Atomic cobalt on nitrogen-doped graphene for hydrogen generation.

 Nature Communications 2015, 6, 8668.
- 21. Hou, H.; Mao, J.; Han, Y.; Wu, F.; Zhang, M.; Wang, D.; Mao, L.; Li, Y. Single-atom electrocatalysis: a new approach to in vivo electrochemical biosensing. *Science China Chemistry* 2019, 62, 1720-1724.
- Pan, Y.; Lin, R.; Chen, Y.; Liu, S.; Zhu, W.; Cao, X.; Chen, W.; Wu, K.; Cheong, W.-C.; Wang, Y.; Zheng, L.; Luo, J.; Lin, Y.; Liu, Y.; Liu, C.; Li, J.; Lu, Q.; Chen, X.; Wang, D.; Peng, Q.; Chen, C.; Li, Y. Design of Single-Atom Co-N₅ Catalytic Site: A Robust Electrocatalyst for CO₂ Reduction with Nearly 100% CO Selectivity and Remarkable Stability. *Journal of the American Chemical Society* 2018, 140, 4218-4221.
- 23. Qiu, H. J.; Ito, Y.; Cong, W.; Tan, Y.; Liu, P.; Hirata, A.; Fujita, T.; Tang, Z.; Chen, M. Nanoporous graphene with single atom nickel dopants: An efficient and stable catalyst for electrochemical hydrogen production. *Angewandte Chemie* 2015, 127, 14237-14241.
- 24. Yang, J.; Qiu, Z.; Zhao, C.; Wei, W.; Chen, W.; Li, Z.; Qu, Y.; Dong, J.; Luo, J.; Li, Z.; Wu, Y. In Situ Thermal Atomization To Convert Supported Nickel Nanoparticles into Surface-Bound Nickel Single-Atom Catalysts. *Angewandte Chemie International Edition* 2018, 57, 14095-14100.
- 25. Puurunen, R. L. Surface chemistry of atomic layer deposition: a case study for the trimethylaluminum/water process. *Journal of Applied Physics* 2005, 97, Article No. 121301.

- 26. Wang, X.; Patel, Rajankumar L.; Liang, X. Significant improvement in TiO₂ photocatalytic activity through controllable ZrO₂ deposition. *RSC Advances* 2018, 8, 25829-25834.
- 27. Liang, X.; Lynn, A. D.; King, D. M.; Bryant, S. J.; Weimer, A. W. Biocompatible interface films deposited within porous polymers by atomic layer deposition (ALD). *ACS Applied Materials and Interfaces* 2009, 1, 1988-1995.
- 28. Wang, X.; Donovan, A. R.; Patel, R. L.; Shi, H.; Liang, X. Adsorption of metal and metalloid ions onto nanoporous microparticles functionalized by atomic layer deposition. *Journal of Environmental Chemical Engineering* 2016, 4, 3767-3774.
- 29. Patel, R. L.; Jiang, Y.-B.; Liang, X. Highly porous titania films coated on sub-micron particles with tunable thickness by molecular layer deposition in a fluidized bed reactor. *Ceramics International* 2015, 41, 2240-2246.
- 30. Wang, X.; Zhao, H.; Wu, T.; Liu, Y.; Liang, X. Synthesis of highly dispersed and highly stable supported Au-Pt bimetallic catalysts by a two-step method. *Catalysis Letters* 2016, 146, 2606-2613.
- 31. Mock, S. A.; Sharp, S. E.; Stoner, T. R.; Radetic, M. J.; Zell, E. T.; Wang, R. CeO₂ nanorods-supported transition metal catalysts for CO oxidation. *Journal of Colloid and Interface Science* 2016, 466, 261-267.
- 32. Wang, X.; Jin, Y.; Liang, X. Significant photocatalytic performance enhancement of TiO₂ by CeO₂ atomic layer deposition. *Nanotechnology* 2017, 28, Article No. 505709.
- 33. Sun, T.; Xu, L.; Wang, D.; Li, Y. Metal organic frameworks derived single atom catalysts for electrocatalytic energy conversion. *Nano Research* 2019, 12, 2067-2080.
- 34. Šmit, G.; Zrnčević, S.; Lázár, K. Adsorption and low-temperature oxidation of CO over iron oxides. *Journal of Molecular Catalysis A: Chemical* 2006, 252, 103-106.

- 35. Gao, Q.-X.; Wang, X.-F.; Di, J.-L.; Wu, X.-C.; Tao, Y.-R. Enhanced catalytic activity of α-Fe₂O₃ nanorods enclosed with {110} and {001} planes for methane combustion and CO oxidation. *Catalysis Science & Technology* 2011, 1, 574-577.
- 36. Liu, X.; Liu, J.; Chang, Z.; Sun, X.; Li, Y. Crystal plane effect of Fe₂O₃ with various morphologies on CO catalytic oxidation. *Catalysis Communications* 2011, 12, 530-534.
- 37. Biabani-Ravandi, A.; Rezaei, M.; Fattah, Z. Catalytic performance of Ag/Fe₂O₃ for the low temperature oxidation of carbon monoxide. *Chemical Engineering Journal* 2013, 219, 124-130.
- 38. Cui, L.; Zhao, D.; Yang, Y.; Wang, Y.; Zhang, X. Synthesis of highly efficient α-Fe₂O₃ catalysts for CO oxidation derived from MIL-100 (Fe). *Journal of Solid State Chemistry* 2017, 247, 168-172.
- 39. Wu, P.; Du, P.; Zhang, H.; Cai, C. Graphyne-supported single Fe atom catalysts for CO oxidation. *Physical Chemistry Chemical Physics* 2015, 17, 1441-1449.
- 40. Li, P.; Miser, D. E.; Rabiei, S.; Yadav, R. T.; Hajaligol, M. R. The removal of carbon monoxide by iron oxide nanoparticles. *Applied Catalysis B: Environmental* 2003, 43, 151-162.
- 41. Qi, J.; Chen, J.; Li, G.; Li, S.; Gao, Y.; Tang, Z. Facile synthesis of core–shell Au@CeO₂ nanocomposites with remarkably enhanced catalytic activity for CO oxidation. *Energy & Environmental Science* 2012, 5, 8937-8941.
- 42. Li, Y.; Yu, Y.; Wang, J.-G.; Song, J.; Li, Q.; Dong, M.; Liu, C.-J. CO oxidation over graphene supported palladium catalyst. *Applied Catalysis B: Environmental* 2012, 125, 189-196.
- 43. Wang, Y.-Z.; Zhao, Y.-X.; Gao, C.-G.; Liu, D.-S. Origin of the high activity and stability of Co₃O₄ in low-temperature CO oxidation. *Catalysis Letters* 2008, 125, 134-138.
- 44. Liu, S.; Chen, Y. Enhanced photocatalytic activity of TiO₂ powders doped by Fe unevenly. *Catalysis Communications* 2009, 10, 894-899.

- 45. Zhou, Y.; King, D. M.; Liang, X.; Li, J.; Weimer, A. W. Optimal preparation of Pt/TiO₂ photocatalysts using atomic layer deposition. *Applied Catalysis B: Environmental* 2010, 101, 54-60.
- 46. Zhou, M.; Yu, J.; Cheng, B. Effects of Fe-doping on the photocatalytic activity of mesoporous TiO₂ powders prepared by an ultrasonic method. *Journal of Hazardous Materials* 2006, 137, 1838-1847.
- 47. George, S.; Pokhrel, S.; Ji, Z.; Henderson, B. L.; Xia, T.; Li, L.; Zink, J. I.; Nel, A. E.; Mädler, L. Role of Fe doping in tuning the band gap of TiO₂ for the photo-oxidation-induced cytotoxicity paradigm. *Journal of the American Chemical Society* 2011, 133, 11270-11278.
- 48. Serpone, N.; Lawless, D.; Disdier, J.; Herrmann, J.-M. Spectroscopic, photoconductivity, and photocatalytic studies of TiO₂ colloids: naked and with the lattice doped with Cr³⁺, Fe³⁺, and V⁵⁺ cations. *Langmuir* 1994, 10, 643-652.
- 49. Cao, T.; Li, Y.; Wang, C.; Wei, L.; Shao, C.; Liu, Y. Fabrication, structure, and enhanced photocatalytic properties of hierarchical CeO₂ nanostructures/TiO₂ nanofibers heterostructures.

 *Materials Research Bulletin 2010, 45, 1406-1412.
- 50. Li, G.; Zhang, D.; Jimmy, C. Y. Thermally stable ordered mesoporous CeO₂/TiO₂ visible-light photocatalysts. *Physical Chemistry Chemical Physics* 2009, 11, 3775-3782.

Supporting Information for

Supported Single Fe Atoms Prepared Via Atomic Layer Deposition for Catalytic Reactions

Xiaofeng Wang,^{1,#} Baitang Jin, ¹ Ye Jin,¹ Tianpin Wu,² Lu Ma,² and Xinhua Liang^{1,*}

¹ Department of Chemical and Biochemical Engineering, Missouri University of Science and Technology, Rolla, MO 65409, United States

² X-Ray Science Division, Advanced Photon Source, Argonne National Laboratory, 9700 S. Cass Ave., Argonne, Illinois, 60439, United States

This file includes:

- 1. XAS analysis
- 2. XPS analysis
- 3. XRD analysis
- 4. Raman analysis
- 5. Band gap calculation

Figures S1–S12

Tables S1-S5

E-mail: liangxin@mst.edu (Xinhua Liang)

Dalian 116026, China

^{*}Corresponding author:

^{*} Present address: College of Environmental Science and Engineering, Dalian Maritime University,

1. XAS analysis.

X-ray absorption spectroscopy (XAS), including extended X-ray absorption fine structure spectroscopy (EXAFS) and X-ray absorption near edge structure spectroscopy (XANES), was conducted at bending magnet beamline 9-BM at the Advanced Photon Source (APS), Argonne National Laboratory. The XAS spectra were recorded in transmission mode with the ionization chamber optimized for maximum current with a linear response [5]. Spectra at the Fe K edge (7.0-7.7 keV) were acquired for the Fe/MWCNTs, Fe/SiO₂, and Fe/TiO₂ samples. Fe foil was used to calibrate the monochromator. Standard procedures based on Athena software were used to fit the XAS data.

2. XPS analysis.

The XPS spectra of 25c-Fe/SiO₂ samples (before and after CO oxidation reactions) were recorded with a Kratos Axis 165 X-ray photoelectron spectrometer using monochromatic Al K α radiation (hv= 1486.6 eV), at a take-off angle of 0°. The survey scan spectra and Fe 2p core level spectra were recorded at pass energy of 160 eV and 20 eV, respectively. All binding energy values were corrected to C 1s signal (284.5 eV).

3. XRD analysis.

The crystal structure of Fe/TiO₂ and Fe/SiO₂ samples was detected by X-ray diffraction (XRD) with filtered Cu K α radiation (λ = 1.5406 Å). The scanning range was 2 θ , from 20° to 80°, with a scanning rate of 0.025 °/s. The Scherrer equation was applied to estimate the average crystallite sizes of TiO₂ and Fe/TiO₂ samples: D = $\frac{\kappa\lambda}{B\cos\theta}$, where B is the half-height width of the diffraction peak of anatase, K=0.89 is a coefficient, θ is the diffraction angle, λ is the X-ray wavelength corresponding to the Cu K α irradiation (1.5406 Å), and D is the average crystallite size of the powder sample.

4. Raman analysis.

Raman spectra of TiO_2 and Fe/TiO_2 samples were recorded using a Horiba-Jobin Yvon LabRam spectrometer, equipped with a 17 mW He-Ne laser. Spectra were collected using a $10 \times$ objective lens over a wavenumber range of 200-1200 cm⁻¹. The initial power was 17 mW, as the excitation source. The excitation wavelength used was 632.8 nm, and the filter chosen was 0.6 D. Thus, the

incident power was 6.8 mW. The reported spectra were generated from 10-20 scans of the respective wavenumber range, each taking 10 seconds.

5. Band gap calculation.

The UV-visible diffuse reflectance spectra (DRS) were used to evaluate the band gap of TiO_2 and Fe/TiO_2 samples by plotting $[F(R)*hv]^{1/2}$ against hv, where hv is the energy of the incident photon and F(R) is the reflection in the Kubelka-Munk function [6]. The linear part of the curve was extrapolated to zero reflectance and the band gap energy was derived.

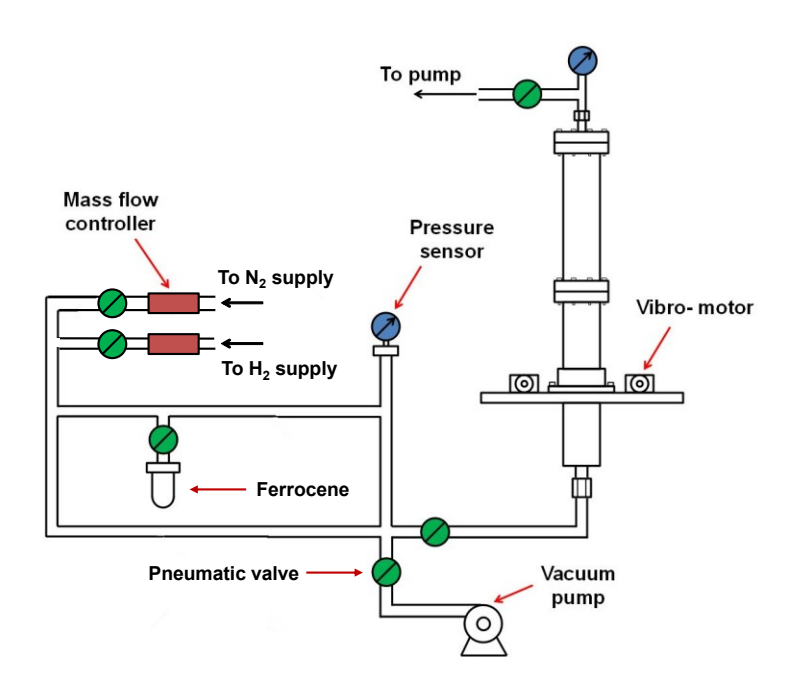


Figure S1. Schematic diagram of an ALD fluidized bed reactor.

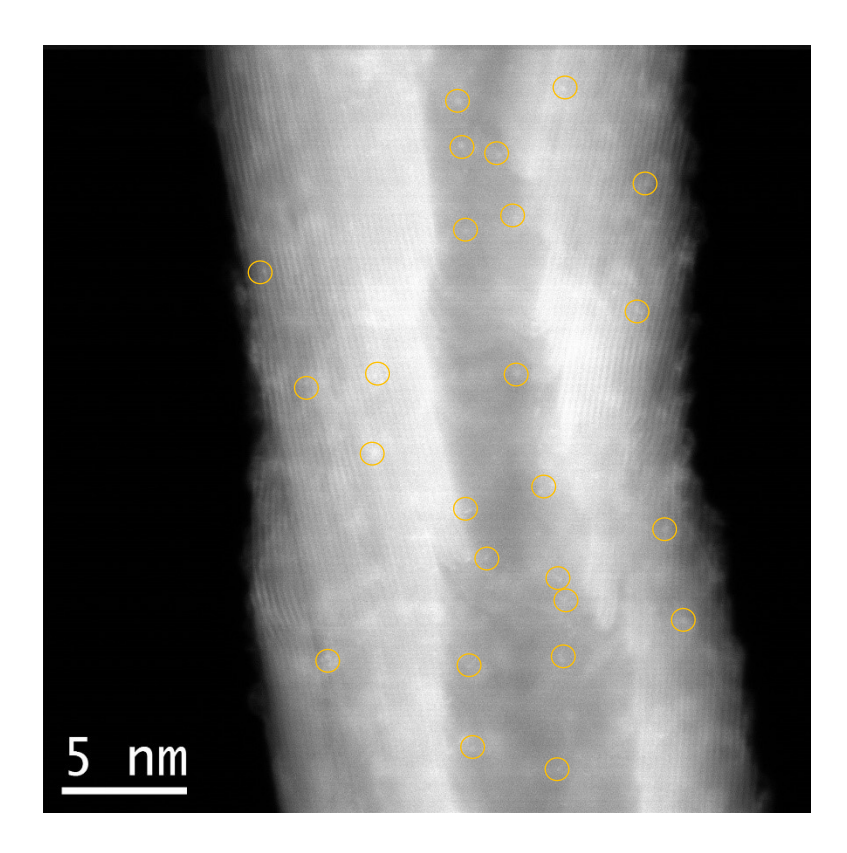


Figure S2. Low magnification HAADF-STEM image of 10c-Fe/MWCNTs.

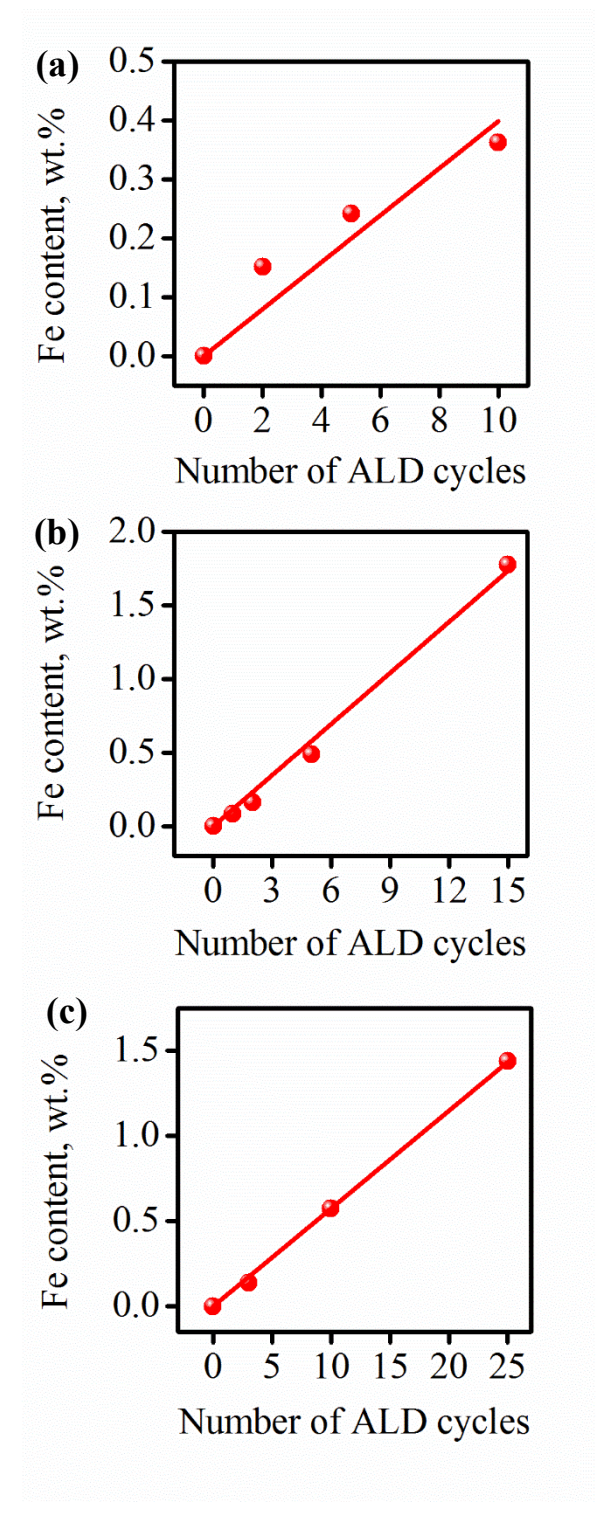


Figure S3. Fe content of (a) Fe/MWCNTs, (b) Fe/TiO₂, and (c) Fe/SiO₂ samples versus the number of Fe ALD cycles.

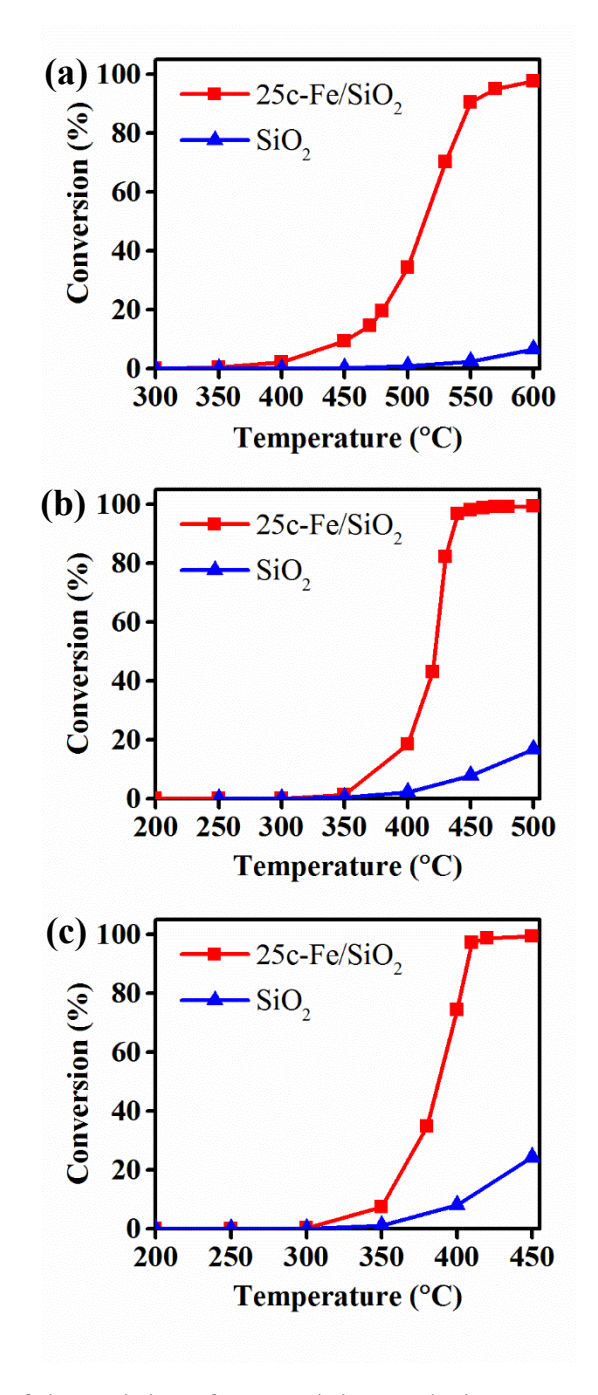


Figure S4. Comparison of the activity of 25c-Fe/SiO₂ and SiO₂ on CO oxidation with different CO:O₂ molar ratios of (a) 1:1, (b) 1:5, and (c) 1:10.

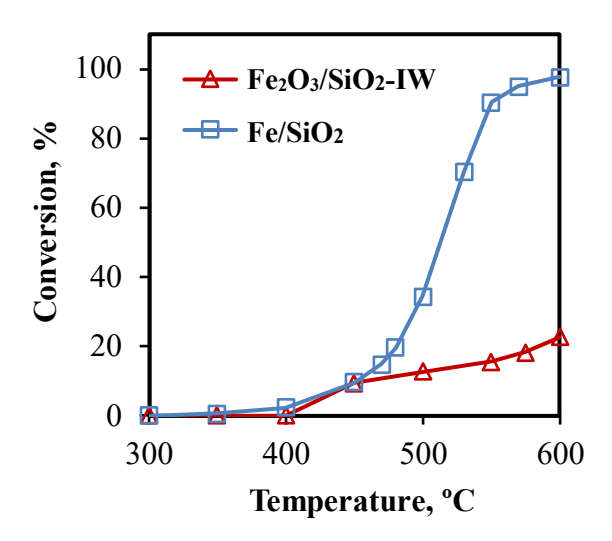


Figure S5. Comparison of Fe₂O₃/SiO₂-IW and 25c-Fe/SiO₂ SAC activity on CO oxidation with a CO:O₂ molar ratio of 1:1.

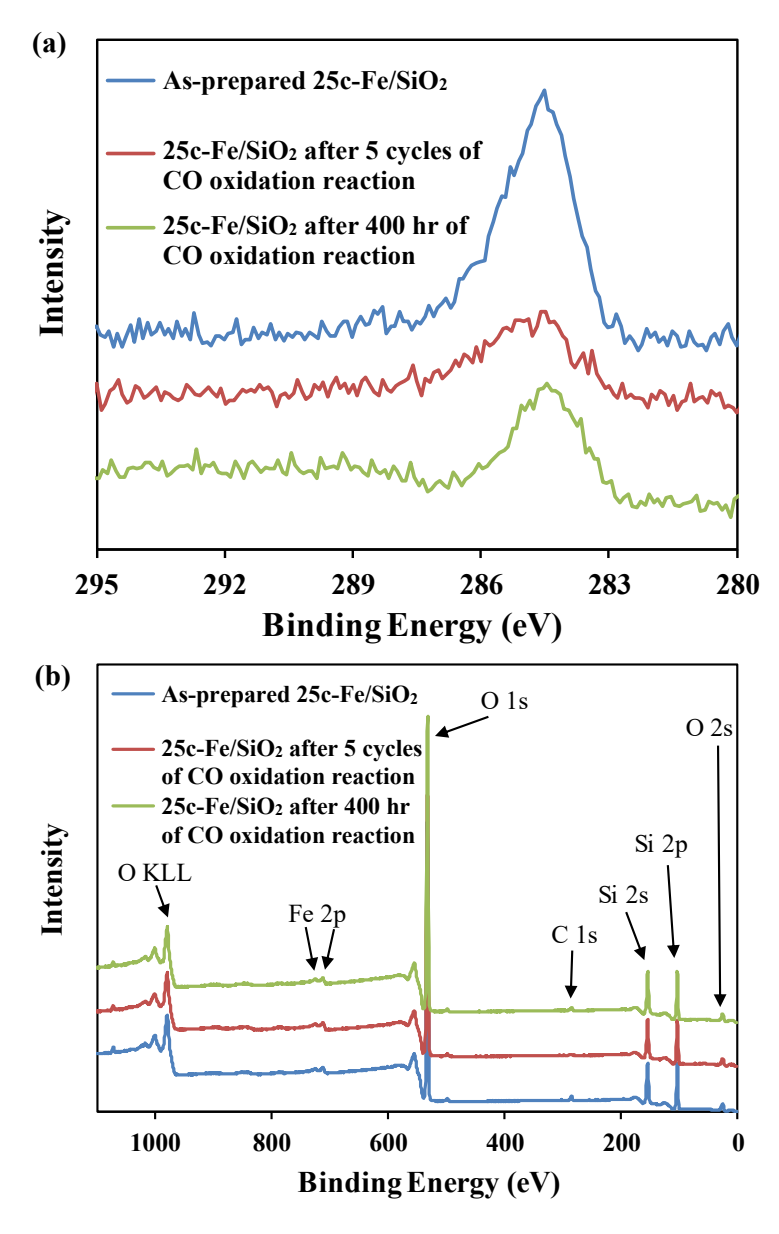


Figure S6. XPS spectra of (a) C (1s) and (b) survey scan for 25c-Fe/SiO₂ SAC before and after CO oxidation reactions.

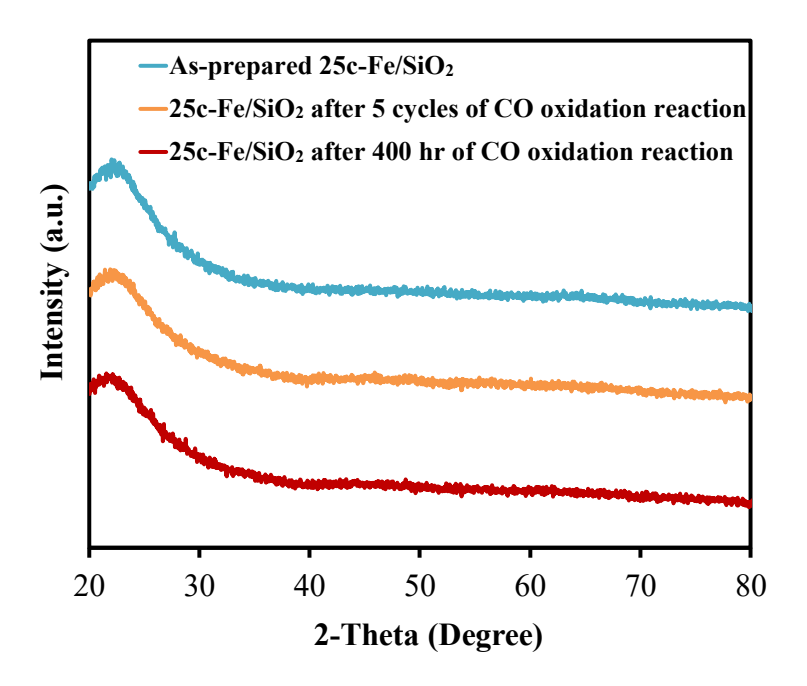


Figure S7. XRD patterns of 25c-Fe/SiO₂ SAC before and after CO oxidation reactions.

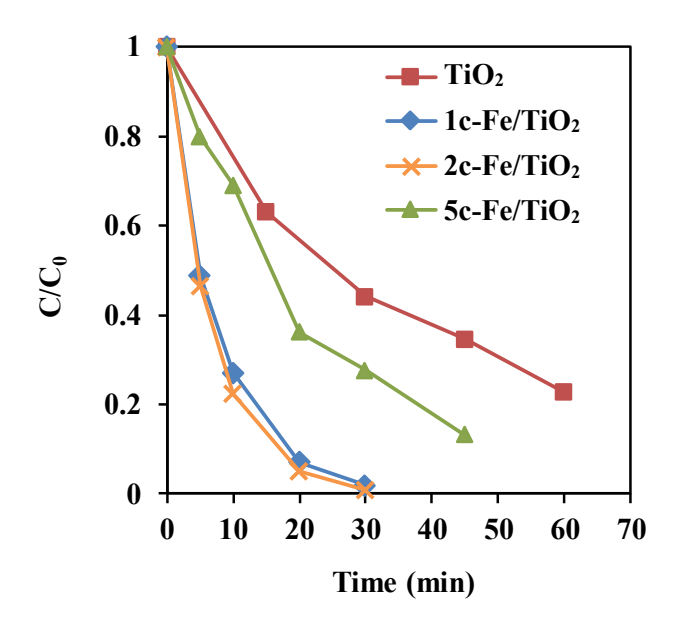


Figure S8. Methylene blue concentration, as a function of UV irradiation time, over different samples.

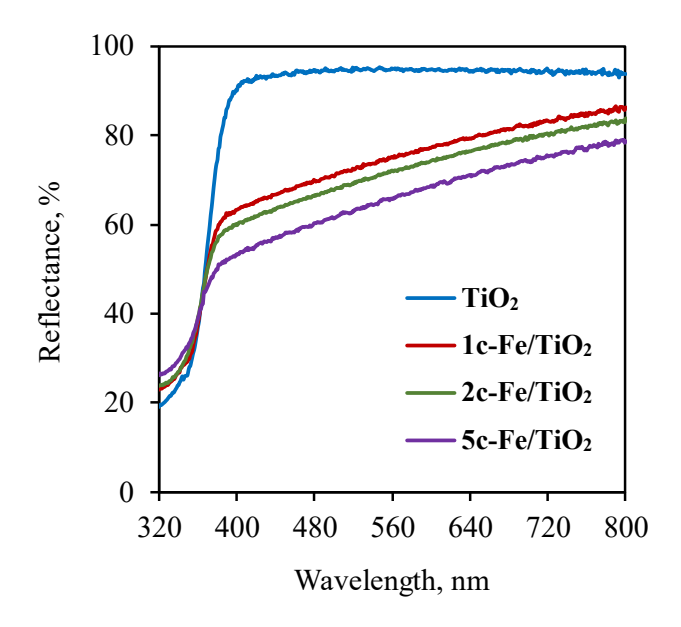


Figure S9. UV-visible reflectance spectra of TiO₂ and Fe/TiO₂ samples.

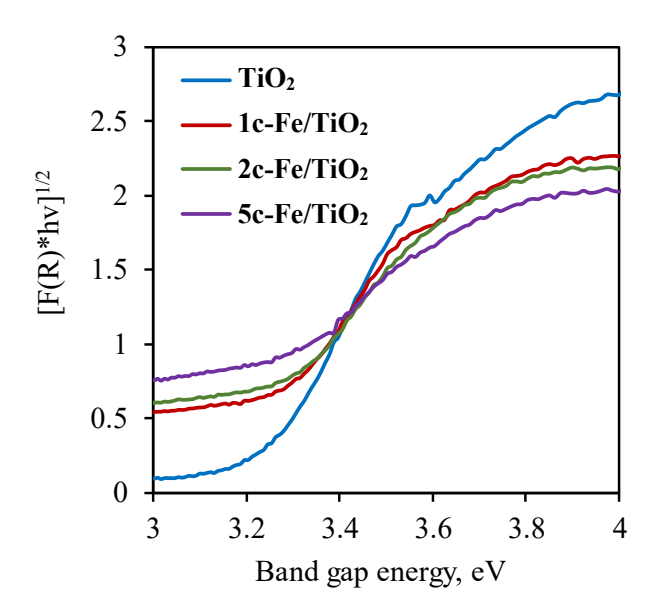


Figure S10. UV-visible spectroscopic measurements and subsequent Kubelka-Munk reflection plots for TiO₂ and Fe/TiO₂ samples.

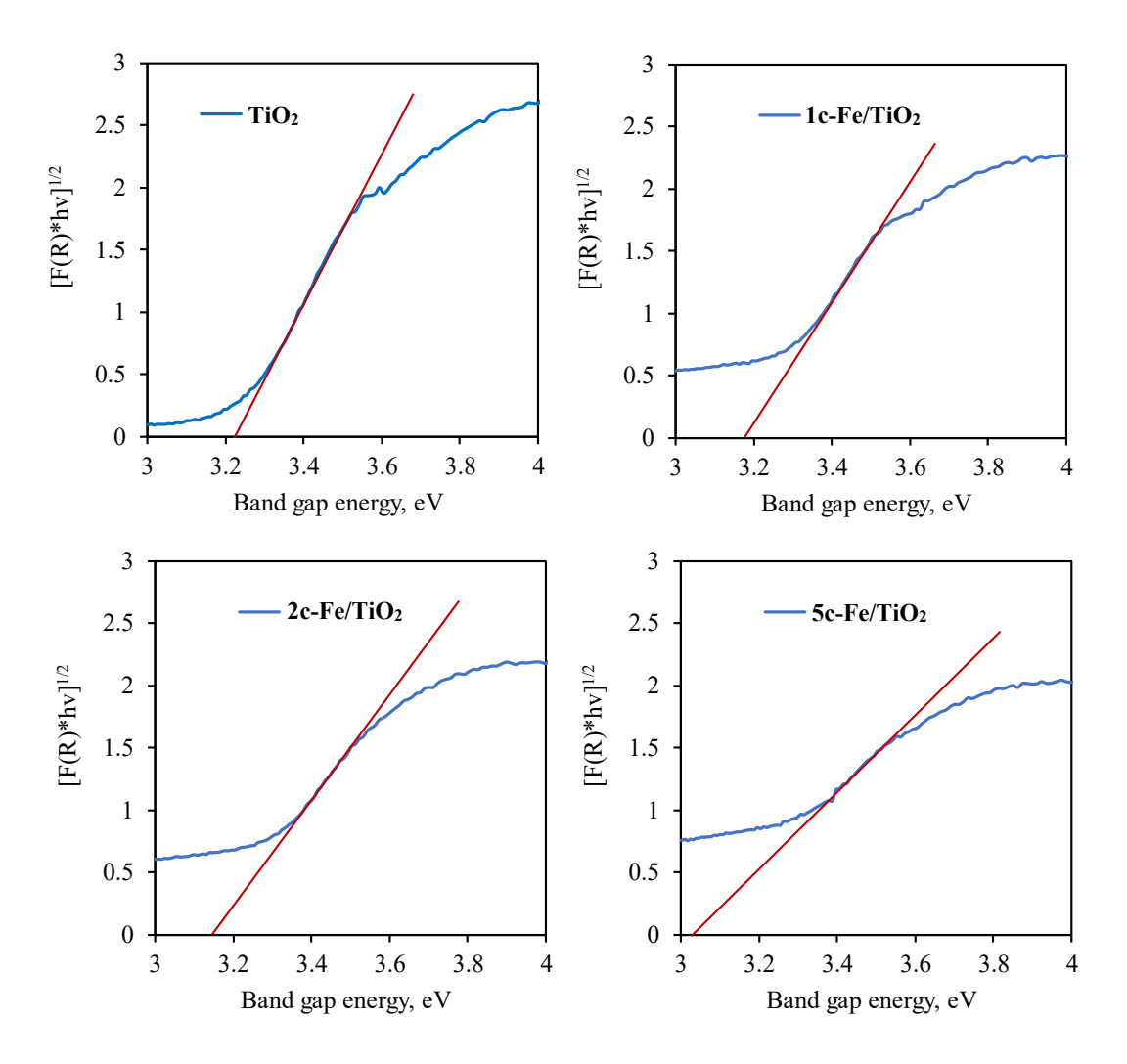


Figure S11. Band gap determination of uncoated TiO₂ nanoparticles and TiO₂ nanoparticles coated with different cycles of Fe ALD. Curved blue and red linear lines represent experimental and extrapolated data, respectively.

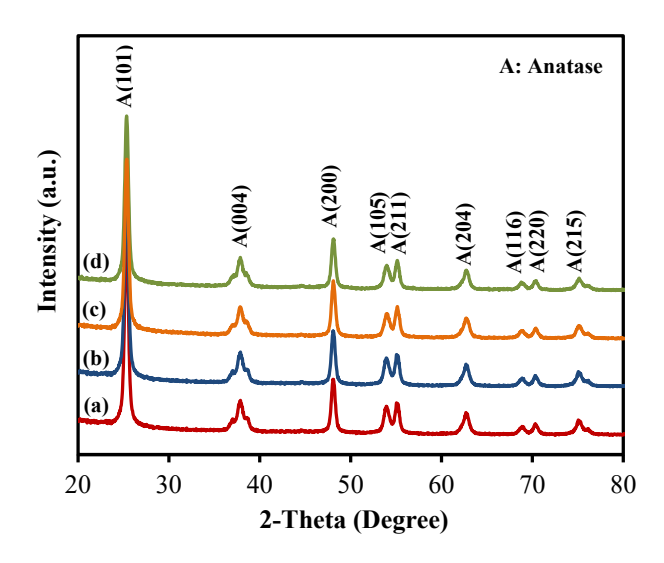


Figure S12. XRD patterns of (a) TiO₂, (b) 1c-Fe/TiO₂, (c) 2c-Fe/TiO₂, and (d) 5c-Fe/TiO₂ samples.

X-ray diffraction (XRD) was used to investigate and determine the effect of Fe deposition on the phase structure. Figure S12 displays the XRD patterns of Fe/TiO₂ samples with different numbers of cycles of Fe ALD. There is no significant difference for any of the samples. The peaks at 25.3°, 37.8°, 48.1°, 53.9°, 55.2°, 62.8°, and 75.2° correspond to the reflections from (101), (004), (200), (105), (211), (204), and (215) planes of TiO₂ in the anatase phase, respectively [2], and no rutile phase was detected in any of the samples. This indicates that the Fe ALD process did not modify the anatase phase of the TiO₂ sample. In addition, no peak corresponds to the reflections from Fe, which could be due to the ultra-small size of Fe on TiO₂. According to the XRD analysis, the TiO₂ crystal size was around 19 nm for all of the samples, which is close to the actual particle size of TiO₂ (~20 nm).

Table S1. Labels of samples and sample descriptions.

	Label of sample	Sample description	Ferrocene dose time (s)
1	2c-Fe/MWCNTs	2 cycles of Fe ALD on MWCNTs	300
2	5c-Fe/MWCNTs	5 cycles of Fe ALD on MWCNTs	300
3	10c-Fe/MWCNTs	10 cycles of Fe ALD on MWCNTs	300
4	1c-Fe/TiO ₂	1 cycle of Fe ALD on TiO ₂	300
5	2c-Fe/TiO ₂	2 cycles of Fe ALD on TiO ₂	300
6	5c-Fe/TiO ₂	5 cycles of Fe ALD on TiO ₂	300
7	15c-Fe/TiO ₂	15 cycles of Fe ALD on TiO ₂	300
8	3c-Fe/SiO ₂	3 cycles of Fe ALD on SiO ₂	300
9	10c-Fe/SiO ₂	10 cycles of Fe ALD on SiO ₂	300
10	25c-Fe/SiO ₂	25 cycles of Fe ALD on SiO ₂	300
11	5c-Fe/SiO ₂ -600s	5 cycles of Fe ALD on SiO ₂	600

Table S2. Valence state of Fe in 15c-Fe/TiO $_2$ and 25c-Fe/SiO $_2$ samples.

	Fe ⁰	Fe ²⁺	Fe ³⁺
15c-Fe/TiO ₂	0	12.3%	87.7%
25c-Fe/SiO ₂	0	14.2%	85.8%

Table S3. Comparison of catalytic activity for CO oxidation on different Fe-based catalysts.

Sample	CO:O ₂	T ₁₀ , °C ^a	T ₅₀ , °C ^b	T ₁₀₀ , °C °	Specific rate _{T100} , $mL_{CO} g_{Fe}^{-1} s^{-1} d$
25c-Fe/SiO ₂	1:10	360	390	410	46.30
FeO_x -200 [8]	1:10	167	240	307	0.48
$Fe_2O_3[9]$	1:10	210	290	420	0.48
Fe ₂ O ₃ nanorods [10]	1:10	230	289	370	0.2
Fe ₂ O ₃ nanocubes [10]	1:10	300	378	580	0.2
Fe ₂ O ₃ nanotubes [10]	1:10	270	400	640	0.2
Fe ₂ O ₃ large cube [11]	1:16	300	470	>500	0.12
Fe ₂ O ₃ large rod [11]	1:16	190	240	280	0.12
Fe ₂ O ₃ -430 [12]	1:20	110	230	253	0.07

^a Temperature (°C) for 10% CO conversion. ^bTemperature (°C) for 50% CO conversion. ^c Temperature (°C) for 100% CO conversion. ^d Volume per second of CO oxidized over per gram of Fe at the temperature for 100% CO conversion.

Table S4. Comparison of long-term stability of CO oxidation for different catalysts.

Sample	Temperature, °C	Time, hr	Decrease of CO conversion, %	References
25c-Fe/SiO ₂	550	>400	0	This work
Pd/graphene	120	24	0	Li et al. [13]
$Au@CeO_2$	120	70	0	Qi et al. [14]
Pd-Au alloy	80	10	2	Xu et al. [15]
Nanoporous Au	30	24	4	Xu et al. [16]
Au-Cu/TiO ₂	20	24	10	Sandoval et al. [17]
Co ₃ O ₄ (LCP- 300)	25	9	20	Wang et al. [18]
Au/Zeolite Y	25	70	27	Chen et al. [19]
Au-Ir/TiO ₂ -S	23	20	60	Gómez-Cortés et al. [20]

 Table S5. Comparison of photocatalytic activity of various samples.

Sample	Preparation method	Pollutant	k _{app} (sample):k _{app} (pure TiO ₂) ^a	References
2c-Fe/TiO ₂	ALD	Methylene blue	6.5	This work
40Ce/TiO ₂	ALD	Methylene blue	3.3	[7]
Pt/TiO ₂	ALD	Methylene blue	3	[21]
0.5% Fe/TiO ₂	Wang et al. [22]	Formaldehyde	3	[23]
4% Fe/TiO ₂	Sol-gel method	Methyl orange	2.0-2.5	[24]
0.25 at.% Fe/TiO ₂	Ultrasonic method	Acetone	1.75	[25]
$0.002~\%~Fe/TiO_2$	Sol-gel method	Methyl orange	1.62	[26]
1.8 at.% Fe/TiO ₂	Sol-gel method	Salicylic acid	1.18	[27]
0.1% Fe/TiO ₂	Hydrothermal method	Methylene blue	<1	[28]

 $^{^{\}text{a}}$ k_{app} is the apparent first order constant.

References

- [1] Liang, X., et al., Biocompatible interface films deposited within porous polymers by atomic layer deposition (ALD). *ACS Applied Materials and Interfaces*, 2009. **1**(9): p. 1988-1995.
- [2] Wang, X., et al., Adsorption of metal and metalloid ions onto nanoporous microparticles functionalized by atomic layer deposition. *Journal of Environmental Chemical Engineering*, 2016. **4**(4): p. 3767-3774.
- [3] Patel, R.L., Y.-B. Jiang, and X. Liang, Highly porous titania films coated on sub-micron particles with tunable thickness by molecular layer deposition in a fluidized bed reactor. *Ceramics International*, 2015. **41**(2): p. 2240-2246.
- [4] Wang, X., et al., Synthesis of highly dispersed and highly stable supported Au–Pt bimetallic catalysts by a two-step method. *Catalysis Letters*, 2016. **146**(12): p. 2606-2613.
- [5] Lei, Y., et al., Synthesis of Pt–Pd core–shell nanostructures by atomic layer deposition: application in propane oxidative dehydrogenation to propylene. *Chemistry of Materials*, 2012. **24**(18): p. 3525-3533.
- [6] George, S., et al., Role of Fe doping in tuning the band gap of TiO₂ for the photo-oxidation-induced cytotoxicity paradigm. *Journal of the American Chemical Society*, 2011. **133**(29): p. 11270-11278.
- [7] Wang, X., Y. Jin, and X. Liang, Significant photocatalytic performance enhancement of TiO₂ by CeO₂ atomic layer deposition. *Nanotechnology*, 2017. **28**(50): p. Article No. 505709.
- [8] Šmit, G., S. Zrnčević, and K. Lázár, Adsorption and low-temperature oxidation of CO over iron oxides. *Journal of Molecular Catalysis A: Chemical*, 2006. **252**(1): p. 103-106.

- [9] Biabani-Ravandi, A., M. Rezaei, and Z. Fattah, Catalytic performance of Ag/Fe₂O₃ for the low temperature oxidation of carbon monoxide. *Chemical Engineering Journal*, 2013. 219: p. 124-130.
- [10] Gao, Q.-X., et al., Enhanced catalytic activity of α-Fe₂O₃ nanorods enclosed with {110} and {001} planes for methane combustion and CO oxidation. *Catalysis Science & Technology*, 2011. 1(4): p. 574-577.
- [11] Liu, X., et al., Crystal plane effect of Fe₂O₃ with various morphologies on CO catalytic oxidation. *Catalysis Communications*, 2011. **12**(6): p. 530-534.
- [12] Cui, L., et al., Synthesis of highly efficient α-Fe₂O₃ catalysts for CO oxidation derived from
 MIL-100 (Fe). *Journal of Solid State Chemistry*, 2017.
- [13] Li, Y., et al., CO oxidation over graphene supported palladium catalyst. *Applied Catalysis B: Environmental*, 2012. **125**: p. 189-196.
- [14] Qi, J., et al., Facile synthesis of core—shell Au@CeO₂ nanocomposites with remarkably enhanced catalytic activity for CO oxidation. *Energy & Environmental Science*, 2012. **5**(10): p. 8937-8941.
- [15] Xu, J., et al., Biphasic Pd–Au alloy catalyst for low-temperature CO oxidation. *Journal of the American Chemical Society*, 2010. **132**(30): p. 10398-10406.
- [16] Xu, C., et al., Low temperature CO oxidation over unsupported nanoporous gold. *Journal of the American Chemical Society*, 2007. **129**(1): p. 42-43.
- [17] Sandoval, A., C. Louis, and R. Zanella, Improved activity and stability in CO oxidation of bimetallic Au–Cu/TiO₂ catalysts prepared by deposition–precipitation with urea. *Applied Catalysis B: Environmental*, 2013. **140**: p. 363-377.

- [18] Wang, Y.-Z., et al., Origin of the high activity and stability of Co₃O₄ in low-temperature CO oxidation. *Catalysis Letters*, 2008. **125**(1-2): p. 134-138.
- [19] Chen, Y.-H., C.-Y. Mou, and B.-Z. Wan, Ultrasmall Gold Nanoparticles Confined in Zeolite Y: Preparation and Activity in CO Oxidation. *Applied Catalysis B: Environmental*, 2017.
- [20] Gómez-Cortés, A., et al., Au-Ir/TiO₂ prepared by deposition precipitation with urea: improved activity and stability in CO oxidation. *The Journal of Physical Chemistry C*, 2009. **113**(22): p. 9710-9720.
- [21] Zhou, Y., et al., Optimal preparation of Pt/TiO₂ photocatalysts using atomic layer deposition. *Applied Catalysis B: Environmental*, 2010. **101**(1): p. 54-60.
- [22] Wang, C.-y., D.W. Bahnemann, and J.K. Dohrmann, A novel preparation of iron-doped TiO₂ nanoparticles with enhanced photocatalytic activity. *Chemical Communications*, 2000(16): p. 1539-1540.
- [23] Dukes, F.M., et al., Differing photo-oxidation mechanisms: electron transfer in TiO₂ versus iron-doped TiO₂. *Langmuir*, 2012. **28**(49): p. 16933-16940.
- [24] Sonawane, R., B. Kale, and M. Dongare, Preparation and photo-catalytic activity of Fe · TiO₂ thin films prepared by sol gel dip coating. *Materials Chemistry and Physics*, 2004. **85**(1): p. 52-57.
- [25] Zhou, M., J. Yu, and B. Cheng, Effects of Fe-doping on the photocatalytic activity of mesoporous TiO₂ powders prepared by an ultrasonic method. *Journal of Hazardous Materials*, 2006. **137**(3): p. 1838-1847.
- [26] Liu, S. and Y. Chen, Enhanced photocatalytic activity of TiO₂ powders doped by Fe unevenly. *Catalysis Communications*, 2009. **10**(6): p. 894-899.

- [27] Popa, M., et al., Synthesis, structural characterization, and photocatalytic properties of iron-doped TiO₂ aerogels. *Journal of Materials Science*, 2009. **44**(2): p. 358.
- [28] Li, Z., et al., Effect of Fe-doped TiO₂ nanoparticle derived from modified hydrothermal process on the photocatalytic degradation performance on methylene blue. *Journal of Hazardous Materials*, 2008. **155**(3): p. 590-594.